# Characteristics of Seismogenic Structures and 3D Stress State of the Delaware Basin of West Texas as Constrained by Earthquake Source Mechanisms

Huang, Guo-chin Dino; Horne, Elizabeth ; Kavoura, Florentia; Savvaidis, Alexandros

**DOI**
10.1785/0220220054

**Publication date**
2022

**Document Version**
Final published version

**Published in**
Seismological Research Letters

# Characteristics of Seismogenic Structures and 3D Stress State of the Delaware Basin of West Texas as Constrained by Earthquake Source Mechanisms

Guo-chin Dino Huang*[1], Elizabeth Horne[1], Florentia Kavoura[2], and Alexandros Savvaidis[1]

## Abstract

**Seismicity in the Delaware basin is suggested to be associated with oilfield operations. To better characterize the seismogenic structures revealed by the induced seismicity, in this study we determined source mechanisms for the Delaware basin of Texas and leveraged the obtained source mechanisms to perform stress inversion for evaluating the region's stress state. Based on the seismogenic patterns and seismicity distribution, we identified seven distinctive seismogenic zones. Within each zone, earthquakes form several parallel-trending linear clusters. Most notably, there is an observable change in the seismicity trend on either side of the basin-bisecting Grisham fault zone. In addition, the extent of hypocentral depths vary drastically across the fault zone, with events located below the basin–basement interface north of the fault zone and more shallowly to the south. We also see spatial variations of source mechanism patterns and the direction of the maximum horizontal stress across the Delaware basin. A vast majority of seismic moment release can be attributed to the basement-rooted tectonic faults in the Culberson–Mentone seismogenic zone. A statistic deficit present in the magnitude–frequency distribution suggests that earthquakes with $M_w$ 3.8–4.7 are needed to fulfill this scaling law. It indicates a strong possibility for future occurrence of earthquakes within this magnitude range.**

**Cite this article as** Huang, G., E. Horne, F. Kavoura, and A. Savvaidis (2022). Characteristics of Seismogenic Structures and 3D Stress State of the Delaware Basin of West Texas as Constrained by Earthquake Source Mechanisms, *Seismol. Res. Lett.* **93**, 3363–3372, doi: 10.1785/0220220054.

**Supplemental Material**

## Introduction

Located in areas across West Texas and southeastern New Mexico, the Delaware basin is well known for its long history of producing vast volumes of hydrocarbons (e.g., shale gas and oil). Significant seismicity in the Delaware basin can be traced back to early 2009 (Frohlich *et al.*, 2020; Skoumal and Trugman, 2021). The recently established Texas Seismological Network (known as TexNet; Savvaidis *et al.*, 2019) has decreased the magnitude of completeness ($M_c$) and improved our knowledge about seismicity in the area. Earthquakes in West Texas are often distributed in spatiotemporally isolated clusters, and the previous studies have provided causative evidence that link hydraulic fracturing (HF) or saltwater disposal (SWD) activities to recent seismicity (Savvaidis *et al.*, 2020; Skoumal *et al.*, 2020; Tung *et al.*, 2020). Changes in pore pressure from the vast volumes of fluids injected through HF and SWD are interpreted to perturb the local stress state around preexisting faults, triggering reactivation (Hennings *et al.*, 2021). Based on well-based framework mapping, 3D seismic data, and prior publications, Horne *et al.* (2021) provided a new map of basement-rooted (BR) fault traces for the Delaware basin and Central Basin Platform. Using similar methods, Horne *et al.* (2022) provided an updated regional interpretation of shallow normal (SN) faults, which are interpreted to be vertically decoupled from the BR set. These extensional features are mapped across the central Delaware basin where a vast majority of the induced earthquakes have occurred and are less extensively mapped north of the Grisham fault zone (GFZ) where recent earthquakes are more spatially aligned with BR faults (Fig. 1a).

At the same time, numerous studies have aimed to define the stress state of the Permian Basin. Lund Snee and Zoback (2018, 2020) had compiled borehole logging data to map the maximum horizontal shear stress ($S_{H\,\max}$) and faulting regime parameters ($A\phi$) across the Permian basin, which have improved our understanding of the stress state of the Delaware basin. However, these works greatly relied on data of borehole loggings, active seismic,

1. Bureau of Economic Geology, The University of Texas at Austin, Austin, Texas, U.S.A., https://orcid.org/0000-0002-6510-2169 (EH); https://orcid.org/0000-0001-6373-5256 (AS); 2. Civil Engineering and Geosciences Faculty, Delft University of Technology, Delft, Netherlands, https://orcid.org/0000-0002-2506-1083 (FK)

*Corresponding author: dino.huang@beg.utexas.edu

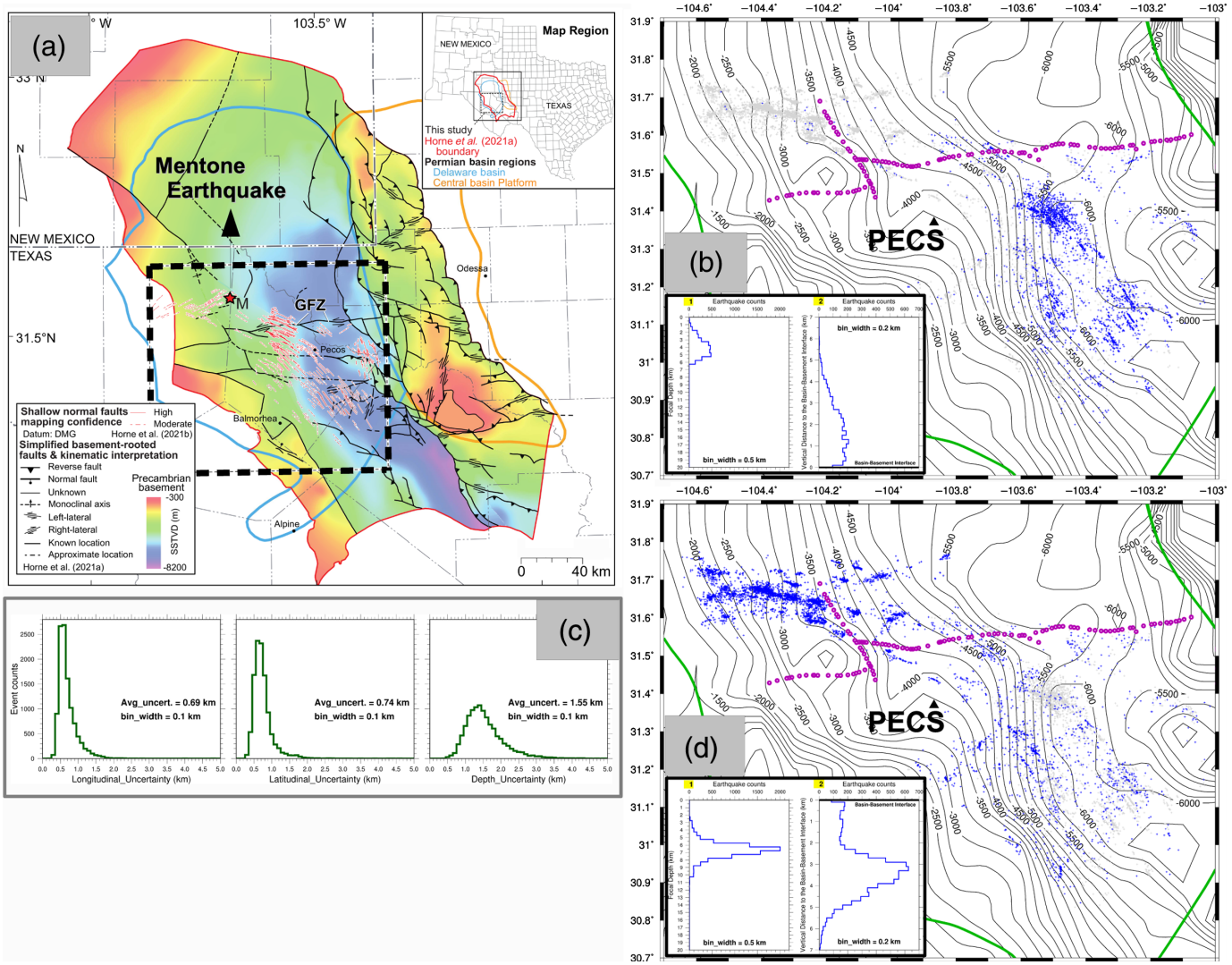


**Figure 1.** Tectonic map and seismicity distribution of the Delaware basin of West Texas. (a) Structure contour map of the faulted Precambrian basement. Macroscale structures and interpreted fault zone kinematic indicators are shown and modified after Horne *et al.* (2021). Interpreted shallow normal faults mapped from Horne *et al.* (2022) are also indicated. See insets for the notations. A red star locates the $M_w$ 4.7 Mentone earthquake, which is by far the largest seismic event ever recorded in Texas by TexNet. (b) Earthquake distribution in the depth range above the basin–basement interface, where the contour lines represent the topography of the interface (Ewing, 1991). The inset shows the statistics of focal depths (inset 1) and their vertical distance to the basin–basement interface (inset 2). The purple dots mark the trace of the Grisham fault zone (GFZ), which is the most significant tectonic feature in our study area. (c) Statistics of hypocentral uncertainty for the relocated earthquakes in our study area. (d) Same convention as that in (b) for earthquakes in the depth range below the basin–basement interface. The color version of this figure is available only in the electronic edition.

and other datasets that have spatial limitations. For example, the stress state is not clear for the depths below the basin–basement interface because of limited number of deep well penetrations. As these earthquakes often occur in preexisting fault systems, the induced seismicity has thus enabled us to uncover unmapped deep seismogenic structures. In addition, earthquake source mechanisms can shed a light on their rupture dynamics. As earthquake sequences developed, it has become clear that understanding the seismogenic system of the basin is of great importance. Until recently, the identification, lateral extent, and role of faults in recent seismicity within the basin was not clear. Nevertheless, the distribution of induced seismicity in the Delaware basin have revealed the presence and depth extent of these previously unknown seismogenic structures. In this article, we aim to investigate the seismogenic pattern of the Delaware basin (Fig. 1). Our approach is to apply these findings to better understand the interaction of fault architecture and seismicity within the basin. To accomplish our goals, we have performed regional waveform moment tensor inversion (referred to as rCMT) to determine earthquake source mechanisms, and applied the obtained source mechanisms to perform regional stress inversion and further determine the orientation of $S_{H\,\max}$. We combined these results to present the characteristics of seismogenic structures for the Delaware basin of Texas.

## Fault Structures and Seismicity of the Delaware Basin

Figure 1 illustrates the simplified, regional fault systems as interpreted by Horne *et al.* (2021, 2022) and the relocated earthquakes hypocenters (January 2017–May 2022; TexNet High Resolution Catalog, 2022) for our study area. Specifically, two prominent geological features are present: the basin–basement interface and the GFZ. The basin–basement interface separates the Precambrian age crystalline rocks and the overlying sedimentary layers. Although its depth varies across the basin, it reaches the deepest in the southeastern Delaware basin at 8 km depth below mean sea level (MSL) (Ewing, 1991; Fig. 1). The GFZ is an east–west-trending fault zone composed of many parallel-trending high-angle segments that accommodated reverse dip-slip and minor left-lateral strike-slip motion (Horne *et al.*, 2021).

**Faults:** The present-day architecture of the region is a product of the combined impacts of multiple extensional and contractional tectonic episodes. These events have constituted a complex fault network composed of both contractile, reverse, as well as normal fault systems. Based on their depth extent, faults in the Delaware basin are separated into two groups of BR faults and SN faults. (1) BR faults are well-developed contractile structures, which formed with and compartmentalized the basin during the Mississippian through Permian age Ancestral Rocky Mountain and Ouachita–Marathon orogenies. The BR faults are expressed along north-northwest–south-southeast-striking faults and generally east–west-striking faults zones, in which north-northwest–south-southeast-striking faults were compartmentalized by east–west-striking faults. This compartmentalization is observed most notably by the GFZ, which bisects the Delaware basin. (2) SN faults are widely observed and mapped across the central Delaware basin. These faults are vertically decoupled from the BR faults and are a product of more recent processes including regional exhumation and potentially anthropogenic influences. These features are clearly observed using 3D seismic reflection datasets (Charzynski *et al.*, 2019; Cook *et al.*, 2019; Hennings *et al.*, 2021), where they are shown to impact only the Cretaceous and uppermost Permian-age strata, however, these features can also be delineated using Interferometric Synthetic Aperture Radar ground deformation grids (Staniewicz *et al.*, 2020).

**Seismicity:** In addition to detecting and locating ambient seismicity on a daily basis, recently the TexNet has conducted an effort to relocate seismicity using GrowClust—a waveform-based correlation method (Trugman and Shearer, 2017), as part of its routine task. The relocation results have been regularly published for better interpretation of seismogenic structures (e.g., TexNet High Resolution Catalog, 2022). The GrowClust used the absolute earthquake locations from published TexNet catalogs as initial locations, along with differential travel times and waveform cross-correlation values, to simultaneously group and relocate events within similar event clusters. As a result, the relocated earthquakes are distributed in several parallel-trending linear clusters (Fig. 1b,d) and appear to be striking in different directions across the GFZ; they trend northwest–southeast south of the GFZ, whereas a slight rotation from northwest–southeast to roughly N60°W–S60°E has occurred in the north of the fault zone. In addition to the change of seismicity trending, the depth extent of seismicity is also different across the GFZ; south of the GFZ, the depth range broadly expands from MSL down to 7 km depth and across the basin–basement interface (the insets of Fig. 1b,d); north of the GFZ, seismicity is in a range of 4–11 km and with high concentration around 7 km depth. A vast majority of them are located 3–3.5 km below the basin–basement interface (inset 2 of Fig. 1d), which is most likely to be related to the reactivation of preexisting BR faults.

## Method of Regional Centroid Moment Tensor Inversion

The Regional Centroid Moment Tensor Inversion (rCMT) algorithm and data processing approach used in this study are based on Huang, Roecker, *et al.* (2017) and Kao *et al.* (1998). We employed a technique developed by Zhu and Rivera (2002) to construct the Green's function database, which takes the near-field term into account and enables us to model small-sized seismic events (e.g., $\mathbf{M} < 3$). A layered 1D velocity model (Huang, Aiken, *et al.*, 2017; Savvaidis *et al.*, 2019; Table S1, available in the supplemental material to this article) is assumed in the Green's function computation. We computed the Green's functions at a sampling interval of 0.02 s, which theoretically sets the Nyquist frequency to be 25 Hz, much higher than the passband we actually used. After computing the Green's functions, moment tensor inversion is performed for each trial hypocenter, followed by generating synthetic waveforms to assess the quality of the moment tensor solution for each trial hypocenter. Our comparison used waveform cross correlation between the observed and synthetic waveforms as a proxy to determine the source mechanism. To avoid the possible cycle-skipping effect from waveform cross correlation, only a small time shift (up to 5 s) is allowed to pursue the minimum waveform misfit. For most cases, the minimum misfit can be achieved by a time shift of less than 2–3 s. As a result, the moment tensor that can minimize the average waveform misfit is considered to be the best-estimated source mechanism.

To ensure reasonable waveform quality for rCMT analysis, seismograms were selected based on visual inspection of waveform quality (e.g., clear presence of surface waves) and the well-distributed azimuthal coverage of recordings on the focal sphere. Various passbands of filters were used to remove background noise, depending on the noise level present when the event occurred. Although an overall lower passband of 0.01–0.1 Hz is commonly used in rCMT analysis (e.g., Huang, Roecker, *et al.* (2017); Kao *et al.*, 1998), this lower passband filtering may have introduced long-period noise for small-sized events (e.g., $M < 3$). After several trial runs on a variety of passbands, we determined

that an overall passband of 0.03–0.8 Hz was suitable. Specifically, the passband can go lower for larger seismic events, whereas it should be higher for smaller events. For example, a passband of 0.03–0.08 Hz was used for an $M_w$ 4.7 event (event 57 in Table S2; Fig. S1), whereas we were able to use a passband of 0.2–0.5 Hz for a $M_w$ 2.3 event (99 in Table S2; Fig. S2). To our best experience, the choice of passband cannot be made exclusively by a simple factor, that is, signal-to-noise ratio (SNR). One can get the highest SNR using an overly narrow and higher passband that may lead to a strong cycle-skipping effect for waveform cross correlation.

## Seismogenic patterns of the Delaware basin

As a result, we have determined 165 source mechanisms that have moment magnitudes ranging from 1.8 to 4.7 (see Table S2). Based on the spatial distribution of seismicity and source mechanism patterns, we have identified seven major seismogenic zones (Fig. 2a–g).

Zone 1 (Fig. 2a): There are 64 source mechanisms with $M_w$ ranging from 2.1 to 4.0 included in this seismic zone, all located below the basin–basement interface. Overall, the events within this zone are determined as normal faulting and with most nodal planes concentrated at N60°W–S60°E. The P axes are commonly near vertical or having steep angles larger than 45°. At the same time, T axes are horizontal or plunged at a shallow angle (<30°) with an overall direction of either due north–south or northeast–southwest. It is worth noting that although the overall seismicity trend of zone 1 is running northwest–southeast, seismicity can be further grouped into several small subclusters. In each subcluster, the seismicity trend is slightly deviated from the general seismicity trend of zone 1.

Zone 2 (Fig. 2b): We have determined 21 source mechanisms in an $M_w$ range of 2.3–4.7, including the largest event ($M_w$ 4.7, event 57 in Table S2) recorded by TexNet since 2017. These events are located much deeper (depth > 6 km), and the preferred nodal planes are striking nearly east–west. Slightly different from that of zone 1, the faulting pattern demonstrates a mix of normal and oblique normal faulting, which can be attributed to five seemingly separated subclusters in zone 2. Nonetheless, the normal component still predominates the faulting process. The P-axes plunge at an angular range from near vertical to 45° and are trending roughly N30°W–S30°E. Meanwhile, T axes are near horizontal or plunged at a shallow angle (<30°). However, they are scattered in a wide range, which can be attributed to the different faulting types in the five isolated subclusters.

Zone 3 (Fig. 2c): Of 25 source mechanisms with $M_w$ = 1.8–3.8 were determined for this zone. They are located across the basin–basement interface and distributed in several isolated subclusters. Although the rupture pattern slightly varies across each subcluster, collectively, the normal-faulting component is still predominant. However, we have observed that the thrust component has increased and is attributed to mostly the presence of vertical dip-slip mechanisms in areas close to the Central Basin Platform (events 5, 11–13, 16–17, 23, and 25). At the same time, both P- and T-axes plunge at medium angles. As a result, these mechanisms have steeper nodal planes, while the preferred nodal plane is striking roughly N50°W–S50°E.

Zone 4 (Fig. 2d): About 11 source mechanisms having $M_w$ 2.3–2.8 were determined in a depth range of 4–7.5 km and distributed in several aligned linear subclusters. Given the fact that the depth to the local basement top is around 5 km, they are crossing the basin–basement interface. The normal-faulting component along with a moderate amount of thrust component dominates the rupture pattern. From these mechanisms, P axes are near vertical or plunged at moderate angles (>45°), while T-axes plunge more shallowly (<30°).

Zone 5 (Fig. 2e): Eight source mechanisms having $M_w$ 2.2–2.9 were determined, and they are distributed in several isolated subclusters. The depth gradient of basin–basement interface is much steeper locally; it is as shallow as 3.2 km in area around event 48, and as deep as 5.5 km around events 88 and 112. The normal-faulting component still dominates the rupture pattern, whereas the involvement of thrust component has however reduced. From these mechanisms, P axes are near vertical or plunged at medium angles, whereas T axes commonly have a shallow dipping angle (<30°).

Zone 6 (Fig. 2f): Of 28 source mechanisms with $M_w$ = 2.2–3.3 were determined for this zone, and they are distributed in several aligned linear subclusters. As a result, although the ambient seismicity in this zone is distributed across the basin–basement interface, the source mechanisms are concentrated mainly at the bottom of the Delaware basin. The normal-faulting component along with a fair amount of thrust component dominates the rupture pattern. From these mechanisms, P axes are near vertical or plunged at steep angles (>60°), whereas T axes commonly have a shallow dipping angle (<30°).

Zone 7 (Fig. 2g): Eight source mechanisms having $M_w$ 2.1–3.0 were determined in several isolated subclusters. Similar to the rupture pattern shown in zones 3, 4, and 6, the normal-faulting component along with a fair amount of thrust component dominates the rupture pattern. From these mechanisms, P axes are near vertical or plunged at steep angles (>60°), whereas T axes commonly have a shallow dipping angle (<30°).

In summary, the normal-faulting component is very predominant across our study area, and there is no fundamental difference of rupture patterns between the basin domain and the crystalline basement top. Nonetheless, we have observed that the thrust component increased in the seismic zones south of the GFZ and geographically close to the Central Basin Platform, resulting in one steep nodal plane from source mechanisms in zones 6 and 7 (Figs. 3b,c, 4f,g). This observation is consistent with the fault mapping results where an apparent system of reverse faults is present (Fig. 1a).

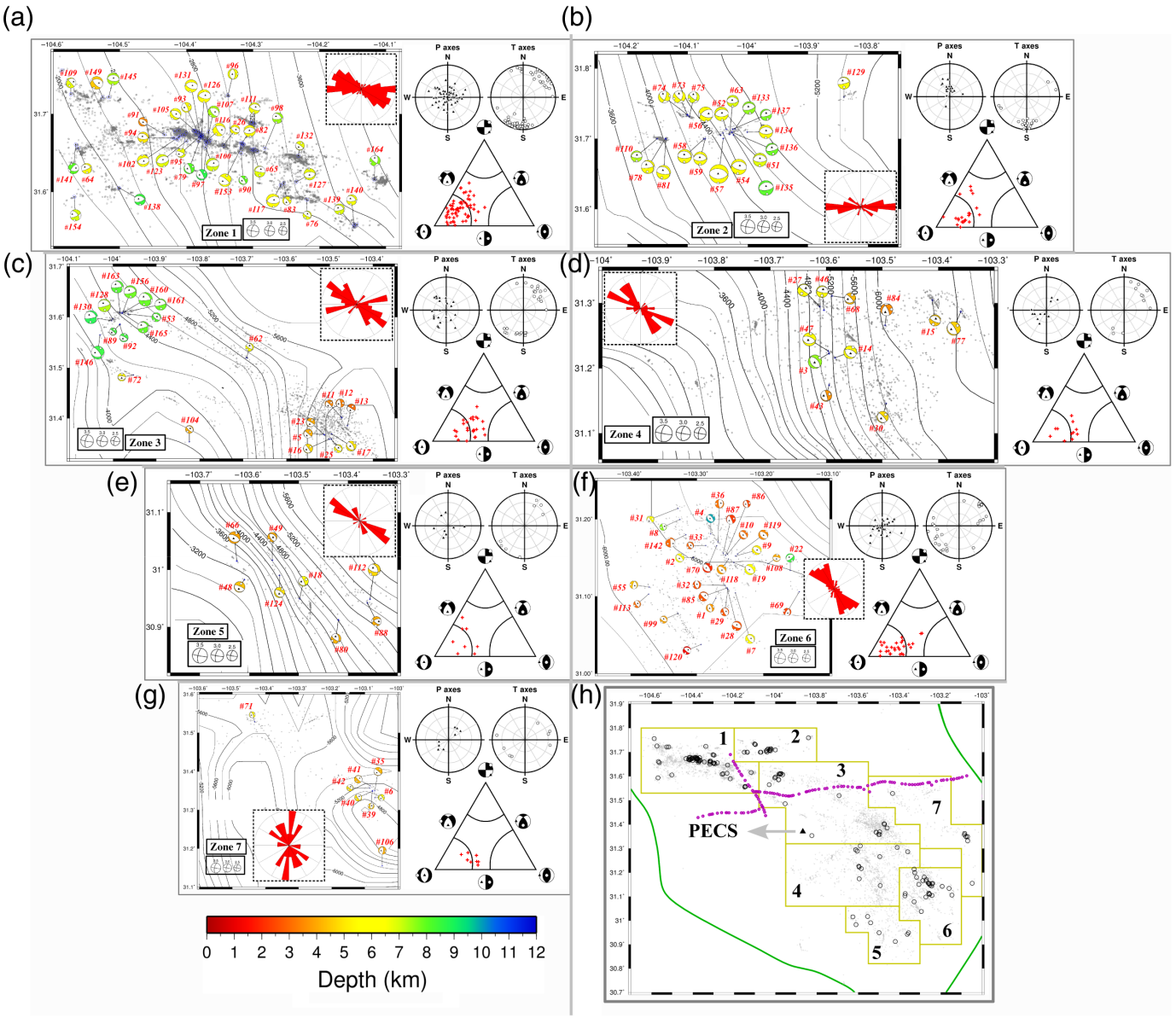


## 3D State of Stress

To assess the stress state across our study area, we employed the Spatial and Temporal Stress Inversion algorithm (Hardebeck and Michael, 2006), and used the source mechanisms obtained from our rCMT analysis to invert for the regional stress field of each seismogenic zone. Considering the tectonic significance of the basin–basement interface, within each seismogenic zone, we further separated the mechanisms into two groups of the basin and the basement top. In addition, we followed the methods developed by Lund and Townend (2007) to estimate $S_{H\,\max}$ from the inverted stress tensors.

As in other geophysical inversion, a proper damper plays a crucial role to stabilize the stress inversion. This parameter can be determined by a trade-off curve between data misfit and model variation. Here, we tested on a series of damping parameters ranging from 0 to 10 at an increment of 0.001 to form the trade-off curve (Fig. S4). Given the fact that the number of available focal mechanisms is not evenly distributed across the seismogenic zones (e.g., 64 focal mechanisms in zone 1 vs. eight focal mechanisms in zone 7), which may lead to an unstable inversion, we chose a number that is slightly higher than suggested by the trade-off curve to suppress the freedom of model variation and pursue a smoother stress model across the region.

**Figure 2.** Seismogenic patterns across seven seismogenic zones in our study area. (a–g) The focal mechanism plots, statistics of nodal planes (i.e., the rose diagrams), the ternary diagrams (Frohlich and Apperson, 1992), and the projections of P and T axes from all source mechanisms in each seismic zone combined. The focal mechanism plots are color coded by events' focal depths, referring to the color table. Each focal mechanism plot is annotated by the number corresponding to their order in Table S2. The size of each focal mechanism plot is also scaled by their $M_w$, see the size reference in each panel. Panel (h) illustrates the boundaries of seismogenic zones. See Seismogenic patterns of the delaware basin section for detailed interpretation. The color version of this figure is available only in the electronic edition.

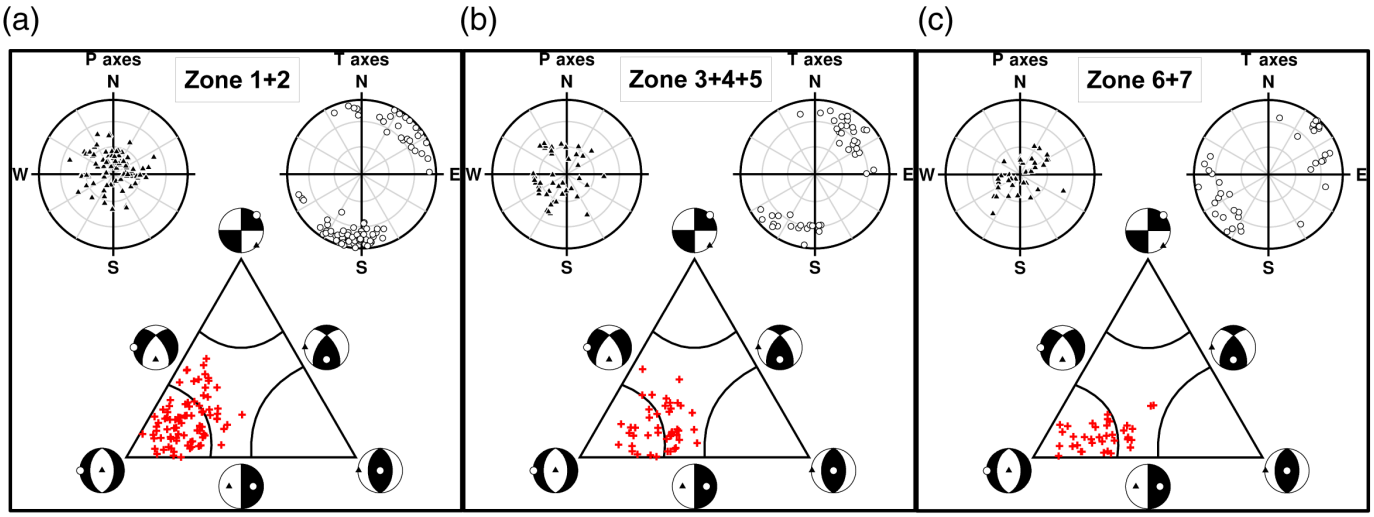


**Figure 3.** Comparison in seismogenic patterns for areas in the north and south of the GFZ. (a) The ternary diagram for seismic zones in the north of the Grisham fault (zones 1 and 2 combined), and the projection of P and T axes from source mechanisms in zones 1 and 2 combined. (b,c) Same diagrams for areas in the south of the Grisham fault, following the same convention shown in (a). They show that the number of oblique-normal mechanisms is reduced from panels (a) to (c), whereas the number of vertical dip-slip mechanisms is increased. Notably, in panel (b), the distribution of the source mechanisms are a little bit scattered, whereas, in panel (c) the source mechanisms are more concentrated in areas close to the side of normal-faulting and vertical dip-slip faulting. All of which suggest that the thrust component has increased in areas south of the Grisham fault, which might be associated with the presence of locally distributed thrust fault near the Central Basin platform, as suggested by the fault mapping results (see also Fig. 1a). The color version of this figure is available only in the electronic edition.

After the stress inversion, following the procedure described by Hardebeck and Michael (2006), we used the bootstrapping approach to evaluate the uncertainty of inversion results. During the trial process on the damping parameters, we have also found that our approach did lead to a smoother model and result in a smaller uncertainty at the best. On average, the azimuthal uncertainty of stress axes is ±18° for S1, ±11° for S2, and ±11° for S3, respectively. At the same time, the average uncertainty of stress axes' plunge is ±3° for S1, ±4° for S2, and ±4° for S3, respectively.

Figure 4 shows that the inverted stress tensors remain a similar fashion across the seismogenic zones, and with no fundamental discrepancy in both the basin and the basement top. In the basin and the basement-top, respectively, we do not see a strong geographic variation of the stress field either. In general, they commonly have horizontal S2 and S3, and vertical S1, indicative of an extensive extensional stress field that led to normal faulting in the shallow crust. However, across the basin–basement interface, the overall direction of S3 has slightly changed from N45°E–S45°W in the basin domain to a range of directions between N30°E–S30°W and N45°E–S45°W in the basement top. As expected, $S_{H\,\max}$ follows the same rotation pattern of stress field, in which the collective orientation has slightly rotated from 135°–150° in the basin to 120°–135° in the basement top. Nevertheless, $S_{H\,\max}$ aligns with the local seismicity trend in each seismogenic zone as expected. All of which suggest that the vertical compressional stress dominates the stress field and results in normal faulting. However, the strike and dip angles of nodal planes are subject to the geometry of preexisting structures.

## Tectonic implication of the Culberson–Mentone seismogenic zone and the role of the Grisham fault

Among these seismogenic zones, seismicity in zones 1 and 2 combined (hereafter referred to as the Culberson–Mentone seismogenic zone [CMSZ]) have recently drawn a particular attention, notably because of the largest event ($M_w$ 4.7) that took place on 26 March 2020 (event 57 in Table S2). Earthquakes in this area have concentrated in the crystalline basement top and interpreted to have occurred along the BR faults (Horne *et al.*, 2021). Although the seismicity rate currently remains high in the CMSZ, it neither alone can exclusively inform the expected earthquake magnitude in the future nor directly translate to the seismic moment release rate. We further combine the seismicity rate and seismic moment release to discuss the magnitude–frequency distribution. We first need to convert $M_L$ (hereafter referred to as $M_{L(TexNet)}$; Kavoura *et al.*, 2020) to $M_w$ for those events we were unable to determine their $M_w$ using rCMT analysis. For this purpose, we established a magnitude scaling law by correlating the obtained rCMT-based $M_w$ with the corresponding $M_{L(TexNet)}$ (Fig. 5a). Instead of the conventional least-squares linear regression, we used orthogonal regression to reduce possible bias due to outliers in the statistics (Shelly *et al.*, 2022). As a result, the scaling law can be defined as

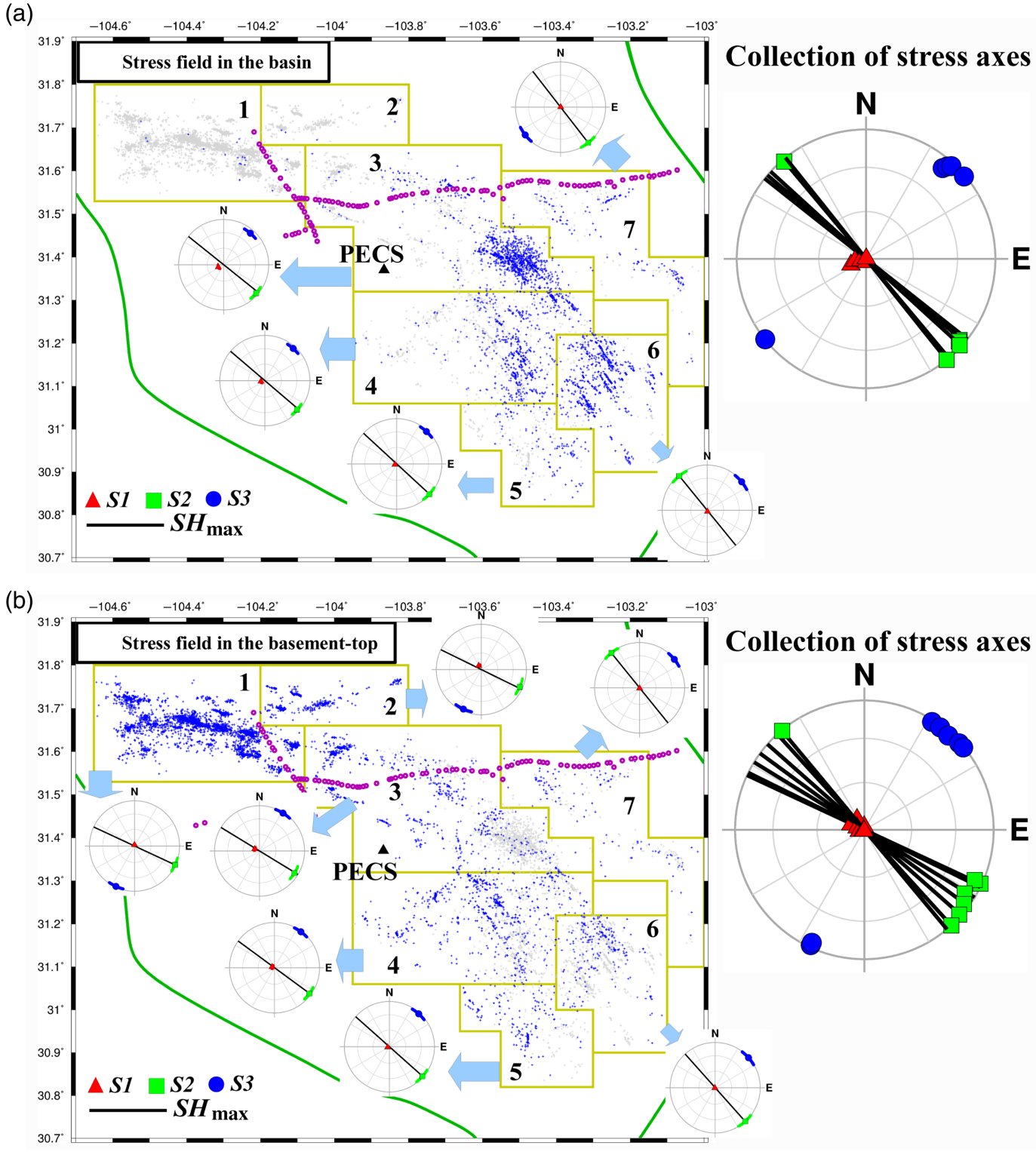


$$M_w = 0.98 \times M_{L(\mathrm{TexNet})} - 0.35, \quad (1)$$

in which the correlation coefficient for the dataset is 0.94. Based on equation (1), we thus estimated rCMT–$M_w$ for the rest of the earthquakes that have no $M_w$ determined by rCMT analysis. We then further converted their estimated

**Figure 4.** The 3D stress map and $S_{H\max}$ calculated for each seismogenic zone for depth ranges in (a) the basin and (b) the basement-top, respectively. See 3D State of stress section for detailed interpretation. The color version of this figure is available only in the electronic edition.

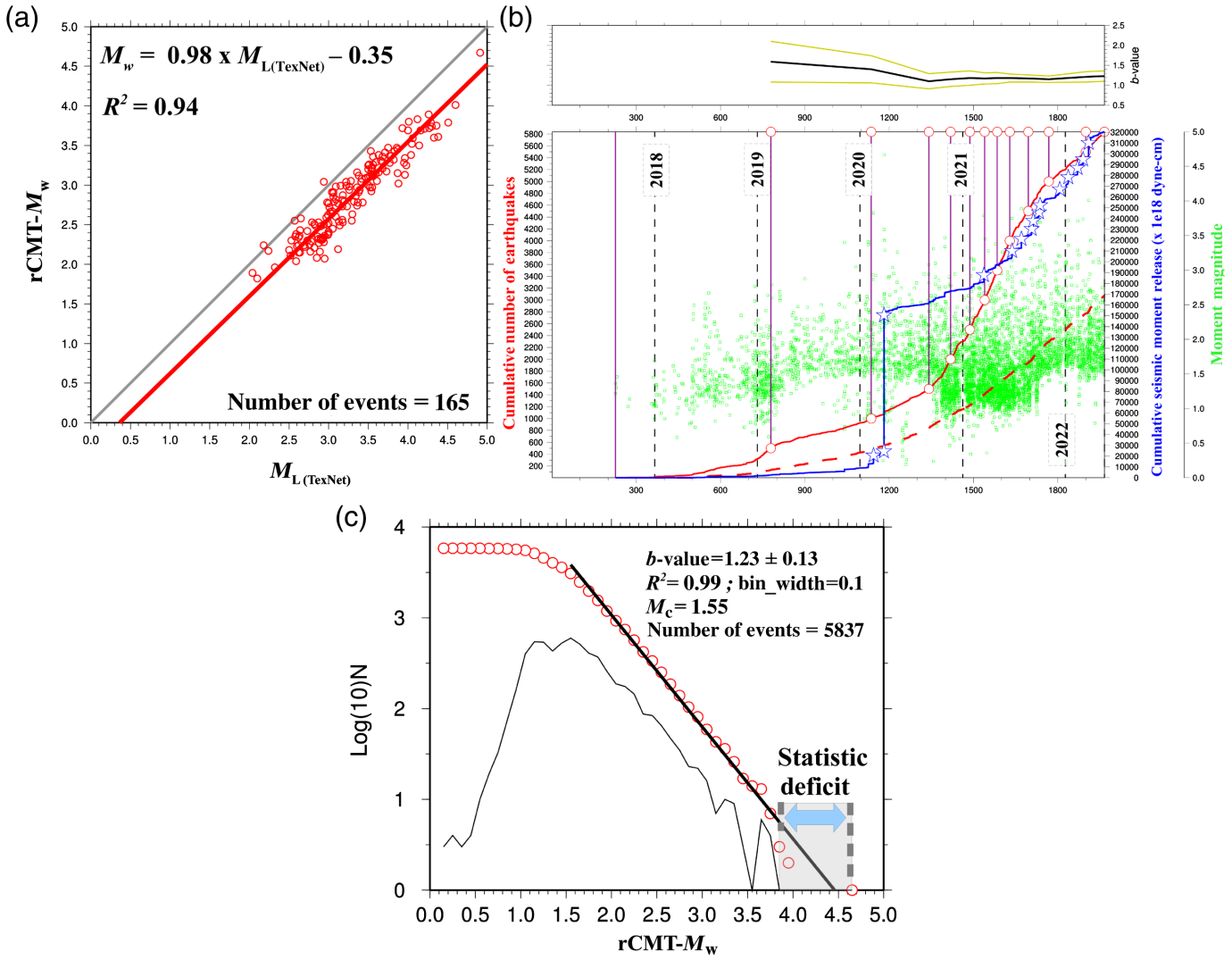


$M_w$ to seismic moment ($M_0$) using the following equation (Hanks and Kanamori, 1979):

$$M_w = \frac{2}{3} \times \log(M_0) - 10.73, \quad (2)$$

in which $M_0$ is in dyn · cm.

Figure 5b demonstrates the relationship between cumulative earthquake numbers (referred to as accumEqk; red line), cumulative seismic moment release (noted as "accumM0"; blue line), as well as the distribution of $M_w$ for each individual event (green diamonds). Results show that accumEqk and accumM0 curves do not have the same development pace, though they commonly consist of several apparent cycles. The accumEqk incrementally increased until mid-2018, and the moment magnitudes are commonly less than 1.8. After mid-2018, the seismicity rate started to rise by adding more events having $M_w > 1.8$, specifically a much higher rate between late 2018 and early 2019. From early 2019 to late 2020, seismicity continues at a steady rate, but the number of $M_w > 3$ events starts to grow. After late 2020, seismicity has once again accelerated

**Figure 5.** (a) Correlation between $M_{L(TexNet)}$ and regional Centroid Moment Tensor (rCMT)-based $M_w$. The red line shows the best-fitting results by orthogonal regression, and the gray line represents the presumed 1:1 ratio of $M_{L(TexNet)}$ to rCMT-based $M_w$. (b) Time-lapse analysis on seismic moment release for the Mentone–Culberson seismogenic zone. The purple lines marks the time span for multiples of 500 events (e.g., 500, 1000, 1500, etc.). Note that the dashed red line represents the cumulative number of earthquakes that have $M_w < M_c$ (1.55, see Fig. 5c). Stars marked on the blue line represent the occurrence of $M_w > 3.5$ events. On the plot of *b*-value variation, yellow lines bound the uncertainty range. (c) Magnitude–frequency analysis for the Mentone–Culberson seismogenic zone. With a suggested optimal bin width of 0.1 (Marzocchi and Sandri, 2003), the $M_c$ was then chosen from the peak value of the $M_w$ histogram. The *b*-value was thus determined accordingly. Results show that accumEqk and accumM0 curves do not have the same development pace, and the *b*-value fluctuates over time. The statistic deficit shown in panel (c) suggests a high probability for a number of earthquakes with $M_w$ 3.8–4.7 to occur in the future, which is needed to fulfill the scaling law. See Tectonic implication of the Culberson-Mentone seismogenic zone and the role of the Grisham fault section for details. The color version of this figure is available only in the electronic edition.

by having more events in a wide magnitude range (e.g., $M_w$ 0.5–4.0). On the other hand, accumM0 did not proportionally add up until late 2019 when $M_w > 3$ earthquakes started to take place. After late 2019, $M_w > 3$ earthquakes frequently occurred in this area and led to the Mentone earthquake sequence in March 2020 (around day 1200 in Fig. 5b). After this sequence, seismicity has become more intense to this day.

As mentioned earlier, seismicity in the CMSZ involves reactivation of BR faults to release tectonic strain. van der Elst *et al.* (2016) have pointed out that induced seismicity hosted by tectonic faults should follow the magnitude–frequency scaling law (Gutenberg and Richter, 1944). The perturbation of pore fluid pressure has a primary control on earthquake triggering, whereas the seismic moment release is subject to only the regional tectonics and the fault network that hosts earthquakes. At the same time, other studies also suggested that *b*-value may fluctuate over time and will gradually return to a level of $b = 1$ or its background level (Bachmann *et al.*, 2012; Huang and Beroza, 2015). To further assess the magnitude–frequency distribution, we used the converted $M_w$ to establish the Gutenberg–Richter scaling law for the CMSZ. The temporal variation of $M_w$ and seismicity statistics have indicated that *b*-value may not be a constant over time, which inspires us to perform time-lapse analysis on *b*-value. Instead of grouping earthquakes primarily by time, we are binning earthquakes by the number at multiples of 500 (e.g., 500, 1000, 1500, etc.), in which every group has a different time span (Fig. 5b). As expected, the *b*-value indeed fluctuates because of the various sizes and numbers of earthquakes over time: it is as high as 1.59 for the first 500 events and as low as 1.10 for 1500 events. We also observe that, over time, *b*-values are elevated by the increase of small-sized events and reduced by the addition of large-sized events. Often, large-sized events occurred when smaller events started to cease. They are therefore combined together to make up several apparent seismogenic cycles.

As a result, we determined *b*-value = 1.23 ± 0.13 out of 5837 earthquakes between January 2017 and May 2022 for the CMSZ. Notably, a statistic deficit of $M_w$ 3.8–4.7 is existing in the magnitude–frequency distribution (Fig. 5c). Earthquakes in this magnitude range are needed to fulfill the scaling law, suggesting a high probability that earthquakes within this $M_w$ range are expected to occur in order to reduce *b*-value to 1 or its background level.

## Conclusion

Our study has shown a spatial variation of source mechanism patterns and stress state across the Delaware Basin of Texas. Although it basically presents extensional faulting in our study area, we observed that the contractional component has slightly increased in areas close to the Central Basin Platform. We believe that localized thrust faults may play a role in the increase of thrust component. At the same time, $S_{H\max}$ slightly rotates across the basin–basement interface in each seismic zone. In each seismic zone, $S_{H\max}$ generally aligns with the local seismicity trend as expected. A vast majority of seismic moment release can be attributed to the reactivation of BR tectonic faults in the CMSZ. The magnitude–frequency analysis for this seismic zone indicates that *b*-value fluctuates over time. Given its tectonic nature, *b*-value will likely reduce toward $b = 1$ by having more larger earthquakes added into the statistics. Specifically, a statistic deficit in the magnitude–frequency distribution implies a high possibility for future occurrence of earthquakes with $M_w$ 3.8–4.7 to fulfill the scaling law. The seismogenic pattern displayed in the CMSZ may reflect the reactivation of BR contractile faults that are experiencing increased perturbation from natural and anthropogenic causes.

## Data and Resources

All seismic waveform data we used can be accessed through either the Data Management Center (DMC) of the Incorporated Research Institutions for Seismology (IRIS) or the Texas Seismological Network (TexNet) webservices of the International Federation of Digital Seismic Networks (FDSN; rtserve.beg.utexas.edu/fdsnws, last accessed June 2022). The supplemental material for this article includes four figures and two tables, see the front page of the supplements for details.

## Declaration of Competing Interests

The authors acknowledge that there are no conflicts of interest recorded.

## Acknowledgments

The authors thank K. Smye of the Bureau of Economic Geology for preparing the depth information of the basin–basement interface for this study. Seismic data used in this study were processed using Seismic Analysis Code (SAC) software. All maps were generated using Global Moment Tensor (GMT) software (Wessel and Smith, 1991). This article benefited from constructive comments made by two anonymous reviewers. Publication of this article was authorized by the Director of the Bureau of Economic Geology, University of Texas at Austin.

## References

Bachmann, C. E., S. Wiemer, B. P. Goertz-Allmann, and J. Woessner (2012). Influence of pore-pressure on the event-size distribution of induced earthquakes, *Geophys. Res. Lett.* **39,** L09302, doi: 10.1029/2012GL051480.

Charzynski, K., K. Faith, Z. Fenton, A. Shedeed, M. McKee, S. Bjorlie, and M. Richardson (2019). Delaware basin horizontal Wolfcamp case study: Mitigating H2S and excessive water production through isolating densely fractured intervals correlative to seismically mapped shallow graben features in the Delaware Mountain Group, *Proc. of the 7th Unconventional Resources Technology Conf.*, American Association of Petroleum Geologists, Tulsa, Oklahoma, doi: 10.15530/urtec-2019-1037.

Cook, S., M. McKee, and S. Bjorlie (2019). Delaware basin horizontal Wolfcamp case history: HTI fracture analysis to avoid H2S and extraneous water linked to Graben features, *Proc. of the 7th Unconventional Resources Technology Conf.*, American Association of Petroleum Geologists, Tulsa, Oklahoma, doi: 10.15530/urtec-2019-452.

Ewing, T. E. (1991). The tectonic framework of Texas [accompanying text], in *The Tectonic Map of Texas*,T. E. Ewing (Editor), The University of Texas at Austin, Bureau of Economic Geology, Austin, Texas, 36 pp.

Frohlich, C., and K. D. Apperson (1992). Earthquake focal mechanisms, moment tensors, and the consistency of seismic activity near plate boundaries, *Tectonics* **11,** 279–296.

Frohlich, C., C. Hayward, J. Rosenblit, C. Aiken, P. Hennings, and A. Savvaidis (2020). Onset and cause of increased seismic activity near Pecos, West Texas, United States, from observations at the Lajitas TXAR seismic array, *J. Geophys. Res.* **125,** e2019JB017737, doi: 10.1029/2019JB017737.

Gutenberg, B., and C. F. Richter (1944). Frequency of earthquakes in California, *Bull. Seismol. Soc Am.* **34,** 185–188.

Hanks, T. C., and H. Kanamori (1979). A moment magnitude scale, *J. Geophys. Res.* **84,** 2348–2350.

Hardebeck, J. L., and A. J. Michael (2006). Damped regional-scale stress inversions: methodology and examples for southern California and the Coalinga aftershock sequence, *J. Geophys. Res.* **111,** no. B11, doi: 10.1029/2005JB004144.

Hennings, P., N. Dvory, E. Horne, P. Li, A. Savvaidis, and M. Zoback (2021). Stability of the fault systems that host-induced earthquakes in the Delaware Basin of West Texas and Southeast New Mexico, *Seism. Record* **1,** 96–106, doi: 10.1785/0320210020.

Horne, E. A., P. H. Hennings, and C. K. Zahm (2021). Basement-rooted faults of the Delaware Basin and Central Basin Platform, Permian Basin, West Texas and southeastern New Mexico, in *The Geologic Basement of Texas: A Volume in Honor of Peter T. Flawn*, O. A. Callahan and P. Eichhubl (Editors), The University of Texas at Austin, Bureau of Economic Geology, Austin, Texas, Report of Investigations No. 286, doi: 10.23867/RI0286C6.

Horne, E. A., P. H. Hennings, K. M. Smye, S. Staniewicz, J. Chen, and A. Savvaidis (2022). Structural characteristics of shallow normal faults in the Delaware Basin, *Interpretation* **10,** doi: 10.1190/int-2022-0005.1.

Huang, G.-C. D., C. Aiken, A. Savvaidis, B. Young, and J. Walter (2017). Improving the velocity structure in the Delaware basin of West Texas for seismicity monitoring, *Eos Trans. AGU S23C–0836*, New Orleans, Louisiana, 11–15 December 2017.

Huang, G.-C. D., S. W. Roecker, V. Levin, H. Wang, and Z. Li (2017). Dynamics of intra-continental convergence between the western Tarim basin and central Tien Shan constrained by centroid moment tensors of regional earthquakes, *Geophys. J. Int.* **208,** 561–576.

Huang, Y., and G. C. Beroza (2015). Temporal variation in the magnitude-frequency distribution during the Guy-Greenbrier earthquake sequence, *Geophys. Res. Lett.* **42,** 6639–6646, doi: 10.1002/2015GL065170.

Kao, H., P.-R. Jian, K.-F. Ma, B.-S. Huang, and C.-C. Liu (1998). Moment tensor inversion for offshore earthquakes east of Taiwan and their implications to regional collision, *Geophys. Res. Lett.* **25,** 3619–3622.

Kavoura, F., A. Savvaidis, and E. Rathje (2020). Determination of local magnitude for earthquakes recorded from the Texas Seismological Network (TexNet), *Seismol. Res. Lett.* **91,** 3223–3235.

Lund, B., and J. Townend (2007). Calculating horizontal stress orientations with full or partial knowledge of the tectonic stress tensor, *Geophys. J. Int.* **170,** 1328–1335.

Lund Snee, J.-E., and M. D. Zoback (2018). State of stress in the Permian Basin, Texas and New Mexico: Implications for induced seismicity, *The Leading Edge* **37,** 127–134.

Lund Snee, J.-E., and M. D. Zoback (2020). Multiscale variations of the crustal stress field throughout North America, *Nat. Commun.* **11,** 1951, doi: 10.1038/s41467-020-15841-5.

Marzocchi, W., and L. Sandri (2003). A review and new insights on the estimation of the b-value and its uncertainty, *Ann. Geophys.* **46,** 1271–1282.

Savvaidis, A., A. Lomax, and C. Breton (2020). Induced seismicity in the Delaware basin, West Texas, is caused by hydraulic fracturing and wastewater disposal, *Bull. Seismol. Soc. Am.* **110,** 2225–2241, doi: 10.1785/0120200087.

Savvaidis, A., B. Young, G.-C. D. Huang, and A. Lomax (2019). TexNet: A statewide seismological network in Texas, *Seismol. Res. Lett.* **90,** 1702–1715.

Shelly, D. R., K. Mayeda, J. Barno, K. M. Whidden, M. P. Moschetti, A. L. Llenos, J. L. Rubinstein, W. L. Yeck, P. S. Earle, R. Gok, *et al.* (2022). A big problem for small earthquakes: Benchmarking routine magnitudes and conversion relationships with coda envelope-derived M w in Southern Kansas and Northern Oklahoma, *Bull. Seismol. Soc. Am.* **112,** 210–225.

Skoumal, R. J., and D. T. Trugman (2021). The proliferation of induced seismicity in the Permian Basin, Texas, *J. Geophys. Res* **126,** e2021JB021921, doi: 10.1029/2021JB021921.

Skoumal, R. J., A. J. Barbour, M. R. Brudzinski, T. Langenkamp, and J. O. Kaven (2020). Induced seismicity in the Delaware Basin, Texas, *J. Geophys. Res.* **125,** e2019JB018558, doi: 10.1029/2019JB018558.

Staniewicz, S., J. Chen, H. Lee, J. Olson, A. Savvaidis, R. Reedy, C. Breton, E. Rathje, and P. Hennings (2020). InSAR reveals complex surface deformation patterns over an 80,000 km 2 oil-producing region in the Permian Basin, *Geophys. Res. Lett.* **47,** no. 21, doi: 10.1029/2020GL090151.

TexNet High Resolution Catalog (2022). TexNet High Resolution Catalog, available at https://hirescatalog.texnet.beg.utexas.edu (last accessed June 2022).

Trugman, D. T., and P. M. Shearer (2017). GrowClust: A hierarchical clustering algorithm for relative earthquake relocation, with application to the Spanish springs and Sheldon, Nevada, earthquake sequences, *Seismol. Res. Lett.* **88,** 379–391.

Tung, S., G. Zhai, and M. Shirzaei (2020). Potential link between 2020 Mentone, West Texas M 5 earthquake and nearby wastewater injection: Implications for aquifer mechanical properties, *Geophys. Res. Lett.* **48,** e2020GL090551, doi: 10.1029/2020GL090551.

van der Elst, N. J., M. T. Page, D. A. Weiser, T. H. W. Goebel, and S. M. Hosseini (2016). Induced earthquake magnitudes are as large as (statistically) expected, *J. Geophys. Res.* **121,** 4575–4590.

Wessel, P., and W. H. Smith (1991). Free software helps map and display data, *Eos* **72,** no. 41, 441–446.

Zhu, L., and L. A. Rivera (2002). A note on the dynamic and static displacements from a point source in multi-layered media, *Geophys. J. Int.* **148,** 619–627.

**Manuscript received 22 February 2022**
**Published online 31 August 2022**